J. Biomedical Science and Engineering, 2011, 4, 443-453 **JBiSE**
doi:10.4236/jbise.2011.46056 Published Online June 2011 (http://www.SciRP.org/journal/jbise/).

X-ray digital linear tomosynthesis imaging

Tsutomu Gomi[1], Hiroshi Hirano[2], Masahiro Nakajima[3], Tokuo Umeda[1]

[1]School of Allied Health Sciences, Kitasato University, Sagamihara, Japan;
[2]Department of Radiology, Shinshu University Hospital, Matsumoto, Japan;
[3]Department of Radiology, Dokkyo Medical University Hospital, Koshigaya, Japan.
Email: gomi@kitasato-u.ac.jp

Received 30 April 2011; revised 24 May 2011; accepted 1 June 2011.

ABSTRACT

Aims: The purpose of this review includes the following: 1) to identify indications for volumetric X-ray digital linear tomosynthesis by using a filtered back projection (FBP) algorithm and 2) to compare X-ray digital linear tomosynthesis, X-ray digital radiography, conventional tomography, and computed tomography. Review: The methods include the following: 1) an overview of the tomosynthesis system in comparison with conventional X-ray imaging technology; 2) an overview of the properties of diagnostic imaging for the chest, hip joint, and temporomandibular joint when imaging overlying structures and their effect of various artificial images; and 3) a review of each system. Summary: Tomosynthesis is worthy of further evaluation because of its flexibility and ability to suppress streak artifacts through an appropriate choice of an FBP algorithm. Tomosynthesis may be considered the imaging technique of choice for investigation of bone changes and detection of pulmonary nodules. Understanding the potential of tomosynthesis imaging will improve diagnostic accuracy in clinical applications.

Keywords: Tomosynthesis; Temporomandibular Joint; Arthroplasty; Pulmonary Nodules; Dual-Energy Subtraction

1. INTRODUCTION

Interest in tomosynthesis and its clinical applications has been revived by recent advances in digital X-ray detector technology. Conventional tomography technology provides planar information of an object from its projection images. In tomography, an X-ray tube and X-ray film receptor are positioned on either side of the object. The relative motion of the tube and film is predetermined based on the location of the in-focus plane [1]. A single image plane is generated by a scan, and multi-slice computed tomography (CT) scans are required to provide a sufficient number of planes to cover the selected structure in the object. Tomosynthesis acquires only one set of discrete X-ray projections that can be used to reconstruct any plane of the object retrospectively [2]. This technique has been investigated in angiography and imaging of the chest, hand joints, lungs, teeth, and breasts [3-8]. In a review of tomosynthesis by Dobbins *et al.* [9], tomosynthesis was demonstrated to outperform planar imaging to a statistically significant extent.

2. TOMOSYNTHESIS RECONSTRUCTION METHODS

Existing tomosynthesis algorithms can be divided into three categories: 1) backprojection algorithms, 2) filtered backprojection (FBP) algorithms, and 3) iterative algorithms (**Figures 1-3**). The backprojection algorithm is referred to as "shift-and-add" (SAA), whereby projection images taken at different angles are electronically shifted and added to generate an image plane focused at a certain depth below the surface. The projection shift is adjusted so that the visibility of features in the selected plane is enhanced while that in other planes is blurred. Using a digital detector, image planes at all depths can be retrospectively reconstructed from one set of projections. The SAA algorithm is valid only if the motion of the X-ray focal spot is parallel to the detector.

FBP algorithms are widely used in CT in which many projections acquired at greater than 360 degrees are used to reconstruct cross-sectional images. The number of projections typically ranges between a few hundred to about one thousand. The Fourier central slice theorem is fundamental to the FBP theory. In two-dimensional (2D) CT imaging, a projection of an object corresponds to sampling the object along the direction perpendicular to the X-ray beam in the Fourier space [10]. For many projections, information about the object is well sampled and the object can be restored by combining the information from all projections. In three-dimensional (3D) cone-beam imaging, the information about the object in

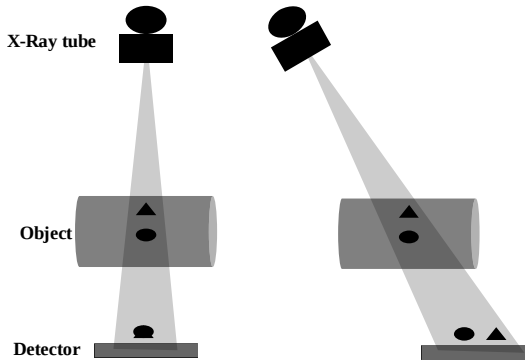

Figure 1. The first view shown here highlights the difficulty in visualizing 3D information in X-ray radiography. In the second view it turns an acquisition direction to avoid superimposition of an object.

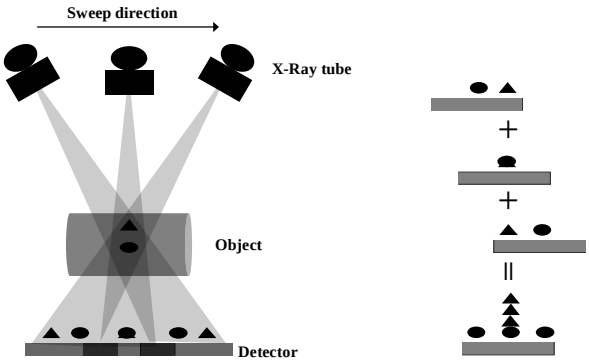

Figure 2. The three resulting projection images may be shifted and added (SAA) so as to bring either the circles or triangles to coincide (*i.e.*, focus), with the complementary object smeared out.

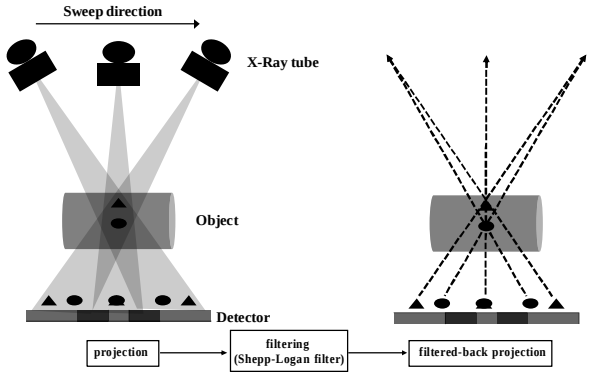

Figure 3. The basis for filtered back-projection (FBP) is the back-projection of data acquired in projections acquired over all angles. This procedure is performed for each pixel in a projection, and for all possible angles of the projected data, then one has created a simple back-projected image of the object.

Fourier space is related to the Radon transform of the object. The relationship between the Radon transform and cone-beam projections has been well studied and solutions to the cone-beam reconstruction have been provided [11,12]. The Feldkamp algorithm (conventional FBP) generally provides a high degree of precision for 3D reconstruction images when an exact type algorithm is employed [13]. Therefore, this method has been adopted for image reconstruction of 3D tomography and multi-detector cone-beam CT. A number of improved 3D reconstruction methods have been derived from the Feldkamp method.

An iterative algorithm performs the reconstruction in a recursive fashion [14,15], unlike the one-step operation in backprojection and FBP algorithms. During iterative reconstruction, a 3D object model is repeatedly updated until the model converges to the solution that optimizes an objective function. The objective function defines the criteria of the reconstruction solution. The objective function in the maximum likelihood (ML) algorithm is the likelihood function, which is the probability of getting the measured projections in a given object model. The solution of the ML algorithm is an object model that maximizes the probability of getting the measured projections.

3. ACQUISITION PARAMETERS

The tomosynthesis system (SonialVision Safire, Shimadzu Co., Kyoto, Japan) consisted of an X-ray tube with a 0.4-mm focal spot and a 432 × 432 mm amorphous selenium digital flat-panel detector. The X-ray collimator was shifted during the acquisition to allow the detector to identify the X-ray illumination area. The motion of the collimator was synchronized with the motion of the tube. An anti-scatter grid was used. The distance from the source to the isocenter was 980 mm and that to the detector was 1100 mm. For detailed estimates of the acquisition parameters, refer to a Table.

4. CONVENTIONAL FBP VS. MODIFIED FBP: EVALUATION OF THE COMPUTER SIMULATION

A previously described modified FBP algorithm provides a description of filtering that can be used in combination with backprojection to yield tomosynthesis slice images with desired properties [16]. The following description of the generalized 3D impulse function was adapted from this previous work [17]. The 3D version of the Fourier slice theorem states that when a 2D image of an object is acquired at a particular orientation to that object, the 2D Fourier transformation of that projection image yields a plane through the 3D Fourier space of the object. Characteristics are estimated in the modified FBP by low-pass filtering processing. The Fourier space low-pass filtering unit applies a low-pass filter along the

Table 1. The detailed estimates of the acquisition paramers.

Digital Linear Tomosynthesis System	
(hip joint, temporomandibular joint)	
Device	SonialVision Safire (Shimadzu Co., Kyoto, Japan)
Source-image-distance (SID)	110 cm
Source-object-distance (SOD)	98 cm
Detector	1024 × 1024 pixels, direct flat-panel detector
Exposure setting	80 kVp, 160 mA, 200 ms/view
Projection and acquisition degree	67 projection, 40 degree acquisition
(chest)	
Device	SonialVision Safire II (Shimadzu Co., Kyoto, Japan)
Source-image-distance (SID)	110 cm
Source-object-distance (SOD)	98 cm
Detector	1280 × 1280 pixels, direct flat-panel detector
Exposure (single-energy acquisition)	120 kVp, 200 mA, 25 ms/view
Exposure (dual-energy acquisition)	60 kVp and 120 kVp, 200 mA, 25 ms/view
Projection and acquisition degree	74 projection, 40 degree acquisition
CT System	
Device	LightSpeed Scanner (GE Medical Systems, Milwaukee, WI, USA)
Data acquisition system (DAS)	0.625 mm × 16 colimation
Exposure setting	120 kVp, 200 mAs/rotation
Reconstruction	MPR images (2 mm slice thickness, 2 mm interval, 580 μm voxel size)
X-Ray Radiographic System	
Device	DigitalDiagnost (Philips Medical Systems, Hamburg, Germany)
Detector	Indirect flat-panel-detector (CsI(Tl))
Exposure setting	70 kVp, 200 mA, 100 ms
Panoramic radiograph & Conventional tomography (for temporomandibular joint)	
Device	Verview Epocs (Morita Co. Tokyo, Japan)
Exposure setting	72 kVp, 3 mAs (panoramic radiograph), 74 kVp, 5 mAs (conventional tomography)

sectional axis of the Fourier space data that have under gone a 3D Fourier transformation. This process is effective in reducing artifacts in the 3D volume data generated by 3D back Fourier transformation of the Fourier space data after low-pass filtering (see appendix A). We performed a computer simulation using a 3D Shepp-Logan phantom, which is defined by 12 solid ellipsoids. This phantom is a simplified model of the human head. The effective X-ray absorption coefficient at any given point is the sum of the relative parameters of the ellipsoids containing that point. The plane locations included the centre and off-centre planes from the location of the object. In the numerical simulation, the 3D Shepp-Logan phantom was used for evaluation by comparing the modified FBP algorithm with the conventional FBP algorithm. The traditional conventional FBP algorithm suffered from a significant decrease in intensity from the mid-plane (**Figure 4**; see "off-centre"), which is a well-known drawback of the conventional FBP algorithm. However, our modified FBP algorithm improved the image quality remarkably and yielded better image quality of both the centre and off-centre planes compared with the conventional FBP algorithm.

5. ACQUISITION PARAMETERS

5.1. CT vs. Tomosynthesis Using Modified FBP

Imaging by X-ray CT has improved over the last three decades and is now a powerful tool in medical diagnostics. CT imaging has become an essential noninvasive imaging technique since the advent of spiral CT imaging in the 1990 s, which led to shorter scan times and improved 3D spatial resolution. CT provides high resolution in the tomographic plane but limited resolution in the axial direction. However, the quality of images generated by a CT scanner can still be reduced due to the presence of metal objects in the field of view. Imaging of patients with metal implants, such as marker pins, dental fillings, or hip prostheses, is susceptible to artifacts generally in the form of bright and dark streaks, cupping and capping, etc. This artifact susceptibility is mostly due to quantum noise, scattered radiation, and beam hardening [18]. Metal artifacts influence image quality by reducing contrast and by obscuring details, thus impairing the ability to detect structures of interest and possibly leading to misdiagnosis. In addition, CT values are impaired, which can lead to errors when using these data e.g., for

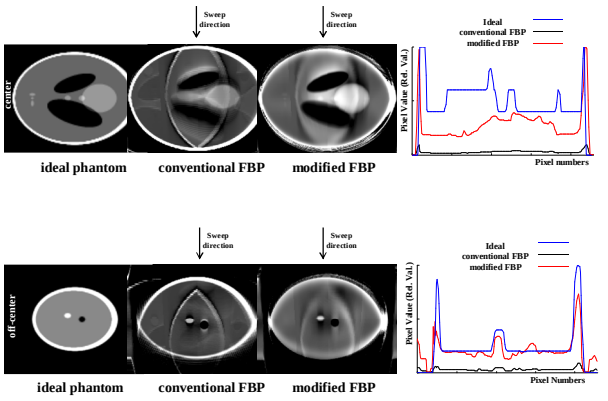

Figure 4. Reconstruction simulation images of the three-dimensional (3D) Shepp-Logan phantom at different heights. In addition, comparison of axial profile plots through the reconstructed 3D image function in comparison with discretization of the 3D Shepp-Logan phantom (centre and off-centre planes).

attenuation correction in PET/CT imaging [19]. The metallic components of arthroplasty devices are high-contrast objects that generate artifacts when imaged using CT scans. These artifacts can make it extremely difficult or impossible to interpret images obtained by devices. The presence of artifacts along with PVE severely limits the potential for objective quantification of total joint replacement with CT.

Methods for reduction of metal artifacts aim to improve the quality of images affected by these artifacts. In recent years, modified iterative [20-23] or wavelet reconstruction techniques [24] have produced promising results. However, these methods cannot be combined with the fast and robust FBP algorithm, which is the standard reconstruction technique implemented in modern CT scanners.

Digital linear tomosynthesis using the modified FBP algorithm shows adequate overall performance, but its effectiveness depends strongly on the region of the image. Digital linear tomosynthesis using modified FBP algorithm images gives good results independent of the type of metal present in the patient and shows good results for the removal of noise artifacts, especially at greater distances from metal objects. Application of digital linear tomosynthesis to the imaging of hip prostheses appears promising. In addition, flexibility in the choice of digital linear tomosynthesis imaging parameters based on the desired final images and generation of high quality images may be beneficial (**Figure 5**).

5.2. Metal Artifact Reduction for Prosthesis Imaging

Metal artifacts influence image quality by reducing contrast and obscuring detail, thus impairing the ability to detect structures of interest and making diagnosis impossible. The objective of this report is to evaluate the clinical application of digital linear tomosynthesis in imaging a phantom and hip prosthesis using a relatively new tomosynthesis instrument and applying a selection of reconstruction algorithms. Tomosynthesis images were compared with the results from artifact reduction processing and a conventional FBP algorithm.

Artifacts caused by high-attenuation features in hip prostheses were observed in digital linear tomosynthesis reconstruction as a result of the small number of projections and narrow angular range typically employed in tomosynthesis imaging. Gomi *et al*. [25] developed artifact reduction methods based on a modified Shepp- Logan reconstruction filter kernel by taking into account the additional weight of direct current components in the frequency domain space. Processing leads to an increase in the ratio of low frequency components in an image (**Figure 6**, see appendix B). Artifact reduction process-

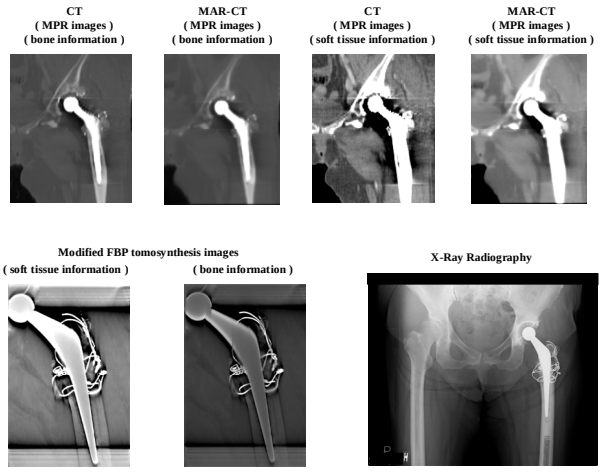

Figure 5. Patient (52-year-old woman; total hip arthroplasty; THA). Anteroposterior (AP) radiographs of the hip and knee joint prostheses are demonstrated. AP radiograph of these joints demonstrate the excellent visualization of the prostheses in this view. AP radiograph is difficult to visualize 3D information in an AP radiograph as shown. Coronal slice images of the hip prosthesis at center heights on Metal Artifact Reduction (MAR) CT (MAR-CT) and non MAR-CT scans at approximately the same level. Remarkable metal artifacts can be seen occurring in the neighborhood of the hip prosthesis. However, MAR-CT processing reduced the metal artifacts. Tomosynthesis images of the prostheses at center heights at the same level. The new diagnostic information that could not be acquired from CT images is provided. Reduction in metal artifacts was obtained in the images as shown here. The use of tomosynthesis allowed better visualization of the prosthesis caused by the blurring of anatomic structures above and below the visualized planes.

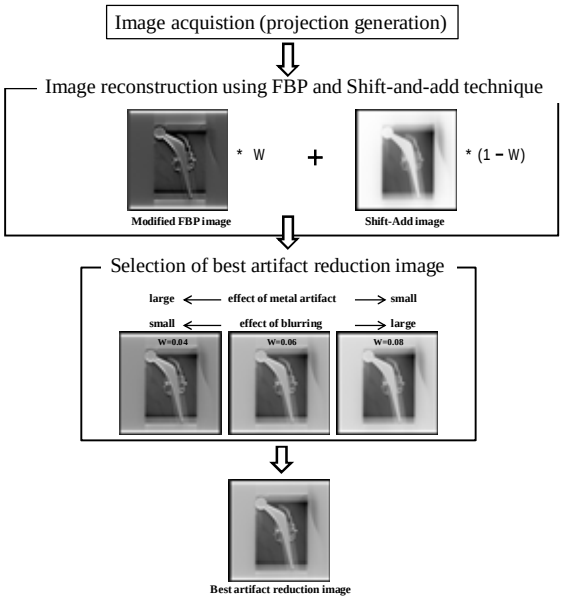

Figure 6. Concept of the artifact reduction tomosynthesis method. Artifact reduction tomosynthesis realized by taking into account additional weighting coefficients (W).

ing was performed with a basic and modified FBP algorithm. Artifact reduction processing provides a method of filtering that can be used in combination with the backprojection algorithm to yield sliced images with desired properties by means of tomosynthesis (**Figure 7**).

The quality of CT images is governed by the strength of artifacts, which depends on numerous factors such as size, shape, density, atomic number and position of metal objects, patient size, and patient's cross-section shape. For small implants manufactured from relatively light metals (e.g., titanium), the effects of beam-hardening and scattering are low. Therefore, the corrupted CT values as well as noise-induced streaking artifacts that pose a major problem to image quality can be neglected. In such cases, the digital linear tomosynthesis approach to artifact reduction processing appears to be promising for the reduction of artifacts stemming from metals with a relatively high atomic number.

5.3. Temporomandibular Joint Imaging

Since the discovery of X-rays in 1895 and their application to dentistry, radiographic imaging of oral anatomy has consisted primarily of viewing 3D structures projected onto a 2D plane. This form of imaging, known as radiography, is characterized by a point source of radiation producing a beam that passes through the patient and strikes a relatively flat image receptor, which is usually a film. This essentially produces an attenuation map of the structures through which the beam has been transmitted. While the dental profession has relied on this method for obtaining information about the hard tissues of the oral cavity, it inevitably superimposes anatomy and metallic restorations, which confound the problems of identifying and/or localizing diseases or objects in 3D.

The temporomandibular joint is a difficult area to investigate radiographically. A number of imaging techniques have been developed. However, there is no technique that provides accurate imaging of all components of the complex anatomy of the joint. Modern imaging modalities, such as magnetic resonance imaging and CT, including cone-beam CT, are now being used more frequently for radiographic examination by panoramic radiography, conventional tomography, etc., of the temporomandibular joint.

The digital linear tomosynthesis system used here showed adequate overall performance, but it is obvious that its effectiveness is strongly dependent on scan parameters such as tomographic angle, number of views, and section thickness [26,27]. Digital linear tomosynthesis images give good results independent of the type of temporomandibular joint in the patient [28] (**Figure 8**). The potential for application of digital linear tomosynthesis to imaging of the temporomandibular joint appears promising. In addition, flexibility in the choice of digital linear tomosynthesis imaging parameters based on the desired final images and realistic imaging conditions may be beneficial.

The digital linear tomosynthesis images in this study were acquired using linear motion of the X-ray tube and detector. The type of motion used during data acquisition dictates the type of blurring of off-focal-plane objects in the image. Linear motion blurs objects in one dimension only, which leads to linear streak artifacts caused by high-contrast off-focal-plane objects.

6. CHEST IMAGING

6.1. Single-Energy Acquisition

Lung cancer is currently the leading cause of cancer death and continues to be an increasing cause of death worldwide. Due to its high sensitivity, normal-dose helical CT is currently considered the gold standard for

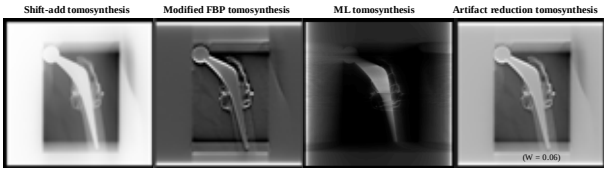

Figure 7. Comparison of images obtained from artifact reduction tomosynthesis (W = 0.06), conventional FBP tomosynthesis, shift-add tomosynthesis, and maximum likelihood tomosynthesis (ML, four subsets & 15 iterations) of the center plane. Artifact reduction tomosynthesis provided better visualization of the hip prosthesis by eliminating blurring and reducing artifacts above and below visualized planes.

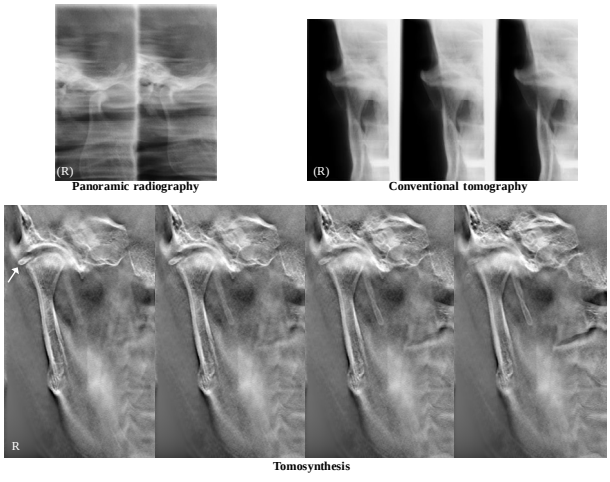

Figure 8. Patient (56-year-old woman; inflammatory disorder of the right temporomandibular joint). Panoramic radiograph (closed and open mouth) showing the mandibular condyle. Conventional tomography showing the right and left mandibular condyle. X-ray digital linear tomosynthesis images (different level positions) showing the mandibular condyle.

lung cancer detection. Early reports indicate that low dose helical CT has the potential to detect early lung cancer, and thus decrease morbidity [29]. CT solves the problem of reduced detection caused by overlapping anatomy. However, there are disadvantages to using CT compared with chest radiography, such as high radiation dose and cost. Advantages of chest radiography include short examination time, low cost, and easy access. However, there are important disadvantages, such as low sensitivity and specificity. In chest radiography, the 3D chest is projected onto a 2D image. Consequently, the ability to detect pathologic findings is limited by the overlapping anatomy rather than by quantum noise. These methods offer much lower sensitivity and specificity than chest radiography as it is practiced currently. Chest radiography has been shown to have relatively low sensitivity for detection of pulmonary nodules. The poor sensitivity for chest radiography precludes its use as a screening modality, despite its advantages of low cost, low dose, and wide distribution of devices. With respect to images of nodules having similar size, the contrast was greater when tomosynthesis imaging was used for processing, as compared with that of radiography [30-32].

Digital linear tomosynthesis is a method that provides some of the tomographic benefits of CT but at a reduced dose and cost and with an approach that is easily implemented in conjunction with chest radiography. Tomosynthesis originates from the older technique of geometric tomography, which has largely fallen out of favor in chest imaging owing to positioning difficulty, high radiation dose, and residual blur from out-of-plane structures. Tomosynthesis overcomes the difficulties of geometric tomography by permitting reconstruction of numerous slices of the image from a single low dose acquisition of image data. Although improving detection of pulmonary masses may be an early area of emphasis for the application of tomosynthesis, it also has potential for use in the thorax.

In addition, there are some limitations with chest tomosynthesis. For example, patients undergoing tomosynthesis have to be able to stand still and hold their breath firmly. Also, chest tomosynthesis has a limited depth resolution, which may explain why pathology in the subpleural region is more difficult to interpret and artefacts from medical devices may occur [33].

6.2. Dual-Energy Acquisition

In the differentiation of benign and malignant pulmonary masses, two radiographic findings give indications of a benign lesion: the presence of calcifications in the mass and stability of the mass [34-38]. A benign pattern of the calcifications has been considered necessary to exclude malignancy [35,39-41]. In the evaluation of diffusely disseminated pulmonary nodules, identification of diffusely disseminated pulmonary nodules and calcifications in the nodules has been helpful in limiting the differential diagnosis [42]. Conventional radiography and conventional tomography have been used to detect calcifications, but they have been largely replaced by CT [36-37].

Dual energy subtraction (DES) imaging has been proposed and investigated by many researchers as a means of reducing the impact of anatomic "noise" on disease detection by chest radiography. DES involves making two radiographic projections of the patient using different energy X-ray beams. By exploiting the difference in the energy dependence of attenuation between bone and soft tissue, the bone contrast can be reduced to produce a soft tissue image and the contrast of the soft tissue can be reduced to produce a bone image [43]. Recent computed radiography (CR) systems have been hampered by poor subtraction effectiveness, workflow inconveniences, and limitations in detective quantum efficiency of the CR technology. DES digital radiography has been found useful in detecting calcifications [35,38,44-47]. Projection images acquired using DES techniques, however, are susceptible to overlap of anatomic features (e.g., calcifications superimposed over the ribs or spine).

DES digital linear tomosynthesis [48] is a new technique (**Figure 9**), and therefore there is no guidance for its integration into the clinical practice of chest radiography. The most reliable signs for discriminating between benign and malignant masses are the growth rate of the mass and presence or absence of calcifications within the mass. Since calcifications are commonly observed in benign masses and no other radiographic characteristic is specific in characterizing a mass, it is important to detect and characterize calcification within lesions. Using DES digital linear tomosynthesis, the presence, distribution, and characteristics of calcifications in lung nodules can be assessed to an extent that is not possible with currently available CT imaging and projection-type DES techniques. In addition, this technique is not susceptible to the problems of image overlap, PVE, or shifting of the image plane (**Figure 10**).

7. POTENTIAL ARTIFACTS

7.1. Blurring

Ideally, structures in a given plane of interest should be clearly displayed in the corresponding tomosynthesis reconstruction plane, whereas structures located outside of that plane should not be visible. Essentially, the limited angular range of the tomosynthesis image acquisition geometry dictates that the spatial resolution is lim-

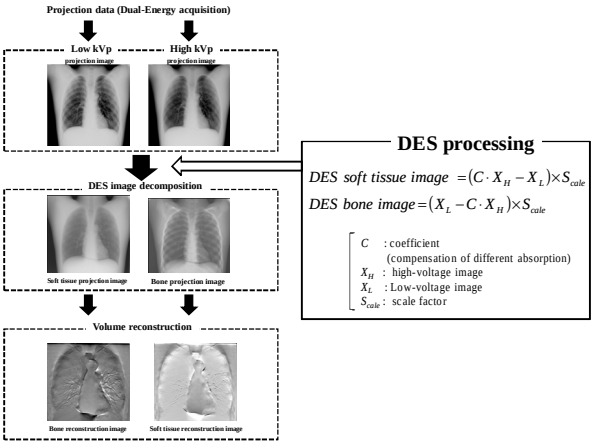

Figure 9. Illustration of the imaging sequence and processing of dual-energy acquisition.

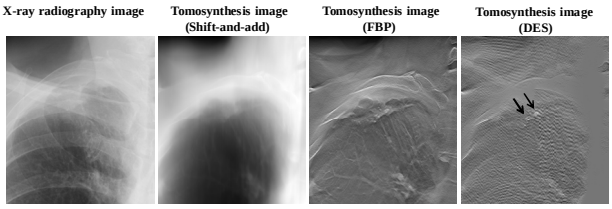

Figure 10. Patient (74-year-old man; calcified tuberculous foci). Comparison of chest images obtained using X-ray radiography, shift-add tomosynthesis, conventional digital tomosynthesis, and dual-energy subtraction digital tomosynthesis. For detection of calcifications in pulmonary nodules, dual-energy subtraction tomosynthesis proved better than any other modality imaging methods.

ited in the dimension perpendicular to the detector plane. As a result, out-of-plane structures cannot be completely removed from the reconstruction plane. Out-of-plane structures are present in every reconstruction plane, but most are not visible because the various low-amplitude structures from projections overlap each other in the reconstruction plane, and therefore are blurred. Out-of-plane structures from high-attenuation features cannot be blurred. They appear as multiple replicates of the particular feature in every reconstruction plane except for the one in which the actual high-attenuation feature is located. At one projection angle, these ghosting features are distributed along the line made by the X-ray source and actual feature (**Figure 11**).

7.2. Ripple

Quantum noise plays an important role in the degradation of contrast resolution of radiographs. It increases inversely with the X-ray exposure and constitutes the dominant noise source at low radiation exposure levels. Because of quantum noise, the technical factors used to reduce radiation dose in our system are limited to those levels usually employed in conventional tomography. However, synthesized tomograms can be obtained with the same technical factors used for radiography when the presence of quantum noise can be tolerated. Any calcifications are visible in the presence of the overwhelmingly rippled artifact on DES digital linear tomosynthesis images (**Figure 12**). This artifact is a consequence of the inherent misalignment between the low and high kVp images because the X-ray tube moves continuously. These features may be amenable to filtration, which may eliminate desired clinical features.

8. FUTURE DIRECTIONS

The digital linear tomosynthesis images in this review were acquired using linear motion of the X-ray tube and detector. The type of motion used during data acquisition dictates the type of blurring of off-focal-plane objects in the image. Linear motion blurs objects in one dimension

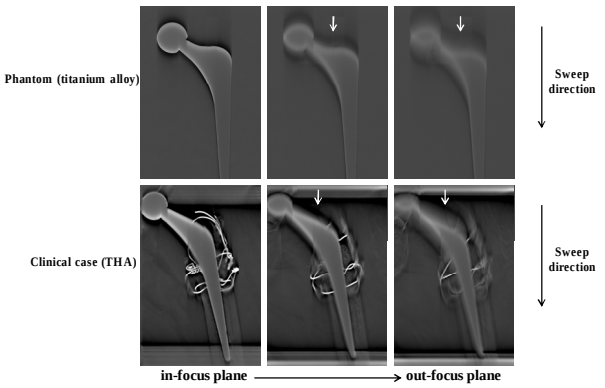

Figure 11. Blurring occurs along the sweep direction and results from imaging studies show that a high contrast structure exists out of the slice plane that is continuously perpendicular to the sweep direction.

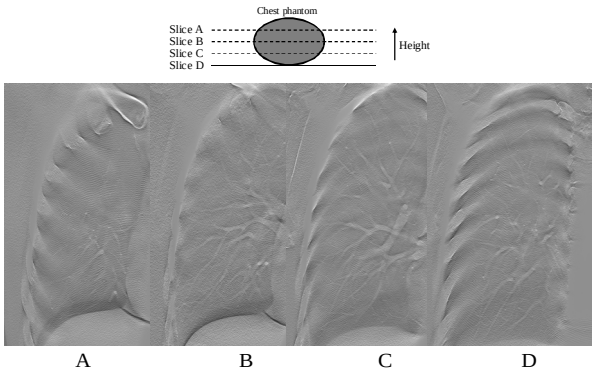

Figure 12. Dual-energy subtraction digital tomosynthesis images of a chest phantom obtained different heights above the dorsal ribs. Blurring changes into ripple as the perpendicular distance from the dorsal ribs to the plane in focus increases above a certain threshold.

only, which leads to linear streak artifacts caused by high-contrast off-focal-plane objects. On the other hand, 3D reconstruction schemes, such as tomosynthesis and CT, require complete knowledge of the X-ray source projection geometry prior to exposure. This limitation precludes much of the potential task-dependent flexibility. This limitation also precludes accurate reconstruction from projections acquired from a patient who moves unpredictably between exposures, as this is geometrically equivalent to not knowing the projection geometry. An alternative approach to tomosynthesis imaging is to determine the number of views that can be acquired given imaging constraints (e.g., time restrictions from patient motion, dose restrictions of the detector). The tomographic angle can be selected to yield images with an acceptable level of artifacts. The tomographic angle then determines the achievable section thickness. This is certainly the case with our modified FBP algorithm (indicated by results presented here) and is suspected to be the case with simple backprojection (or the SAA algorithm). It is possible, however, that this restriction could be reduced by the use of an alternative reconstruction scheme.

Artifact reduction processing showed an adequate overall performance, but its effectiveness strongly depended on the image region. Digital linear tomosynthesis images gave good results independent of the type of metal present in the patient and showed good results for the removal of noise artifacts, particularly at greater distances from metal objects. The potential for application of digital linear tomosynthesis to the imaging of prostheses appears promising. Flexibility in the choice of imaging parameters in artifact reduction processing based on the desired final images and realistic imaging conditions may be beneficial.

Initial data from our study suggest that DES digital linear tomosynthesis will substantially enhance sensitivity and specificity of pulmonary nodule detection. Despite its potential, DES digital linear tomosynthesis is a new technique. Therefore, there is no guidance for its integration into the clinical practice of chest radiography. The most reliable signs for discriminating between benign and malignant masses are the growth rate of the mass and presence or absence of calcifications within the mass. Since calcifications are commonly observed in benign masses and no other radiographic characteristics is specific in characterizing masses, it is important to detect and characterize calcification within lesions. In addition, this technique is not susceptible to the problems of image overlap, PVE, or shifting of the image plane.

9. ACKNOWLEDGEMENTS

We wish to thank for Shimadzu Corporation for her helpful research assistance in this work.

REFERENCES

[1] Ziedses des Plante, B.G. (1932) Eine neue methode zur differenzierung in der roentgenographie (planigraphie). *Acta Radiologica*, **13**, 182-192. doi:10.3109/00016923209135135

[2] Grant, D.G. (1972) Tomosynthesis: a three-dimensional radiographic imaging technique. *IEEE Transactions on Bio-Medical Engineering*, **19**, 20-28. doi:10.1109/TBME.1972.324154

[3] Stiel, G., Stiel, L.G., Klotz, E., *et al*. (1993) Digital flashing tomosynthesis: a promising technique for angiographic screening. *IEEE Transactions on Medical Imaging*, **12**, 314-321. doi:10.1109/42.232261

[4] Warp, R.J., Godfrey, D.G. and Dobbins, J.T. (2000) Applications of matrix inverse tomosynthesis. *Proceedings of SPIE*, **3977**, 376-383.

[5] Duryea, J., Dobbins, J.T. and Lynch, J.A. (2003) Digital tomosynthesis of hand joints for arthritis assessment. *Medical Physics*, **30**, 325-333. doi:10.1118/1.1543573

[6] Sone, S., Kasuga, T., Sakai, F., *et al*. (1995) Image processing in the digital tomosynthesis for pulmonary imaging. *European Radiology*, **5**, 96-101. doi:10.1007/BF00178089

[7] Badea, C., Kolitsi, Z. and Pallikarakis, N. (2001) A 3D imaging system for dental imaging based on digital tomosynthesis and cone beam CT. *Proceedings International Federation for Medical and Biological Engineering*, **2**, 739-741.

[8] Niklason, L.T., Christian, B.T., Niklason, L.E., *et al*. (1997) Digital tomosynthesis in breast imaging. *Radiology*, **205**, 399-406.

[9] Dobbins, J.T. III and Godfrey, D.J. (2003) Digital x-ray tomosynthesis: curent state of the art and clinical potential. *Physics in Medicine and Biology*, **48**, R65-106. doi:10.1088/0031-9155/48/19/R01

[10] Kak, A. and Slaney, M. (1988) Principles of computerized tomographic imaging. IEEE.

[11] Smith, D.B. (1985) Image reconstruction from cone-beam projections: necessary and sufficient conditions and reconstruction methods. *IEEE Transactions on Medical Imaging*, **4**, 14-25. doi:10.1109/TMI.1985.4307689

[12] Grangeat, P. (1991) Mathematical framework of cone-beam 3D reconstruction via the first derivative of the Radon transform. *Math Methods Tomogr*, **1497**, 66-97. doi:10.1007/BFb0084509

[13] Feldkamp, L.A., Davis, L.C. and Kress, J.W. (1984) Practical cone-beam algorithm. *Journal of the Optical Society of America*, **1**, 612-619. doi:10.1364/JOSAA.1.000612

[14] Ruttimann, U., Groenhuis, R. and Webber, R. (1984) Restoration of digital multilane tomosynthesis by a constrained iteration method. *IEEE Transactions on Medical Imaging*, **MI-3**, 141-148. doi:10.1109/TMI.1984.4307670

[15] Bleuet, P., Guillemaud, R., Magin, I., *et al*. (2002) An adapted fan volume sampling scheme for 3D algebraic reconstruction in linear tomosynthesis. *IEEE Transactions on Nuclear Science*, **3**, 2366-2372. doi:10.1109/TNS.2002.803683

[16] Gomi, T. and Hirano, H. (2008) Clinical potential of digital linear tomosynthesis imaging of total joint artroplasty. *Journal of Digital Imaging*, **21**, 312-322. doi:10.1007/s10278-007-9040-9

[17] Lauritsch, G. and Harer, W.H. (1998) A theoretical framework for filtered backprojection in tomosynthesis. *Proceedings of SPIE*, **3338**, 1127-1137. doi:10.1117/12.310839

[18] Hsieh, J. (1995) Image artifacts; causes; and correction. In: Goleman, L.W. and Fowlkes, J.B., Eds., *Medical CT and ultrasound; current technology and applications*, Advanced Medical Publishing, Madison, 487-518.

[19] Kamel, E.M., Burger, C., Buck, A., *et al*. (2003) Impact of metallic dental implants on CT-based attenuation correction in a combined PET/CT scanner. *European Radiology*, **13**, 724-728. doi:10.1007/s00330-002-1564-2

[20] Wang, G., Snyder, D.L., O'Sullivan, J.A., *et al.* (1996) Iterative debluring for metal artifacts reduction. *IEEE Transactions on Medical Imaging*, **15**, 657-664. doi:10.1109/42.538943

[21] Wang, G., Vannier, M.W. and Cheng, P.C. (1999) X-ray coneeam tomography for metal artifacts reduction and local region reconstruction. *Microscopy and Microanalysis*, **5**, 58-65. doi:10.1017/S1431927699000057

[22] Wang, G., Frei, T. and Vannier, M.W. (2000) A fast iterative algorithm for metal artifact reduction in x-ray CT. *Academic Radiology*, **7**, 607-614. doi:10.1016/S1076-6332(00)80576-0

[23] Man, B. De, Nuyts, J., Dupont, P., *et al*. (2000) Reduction of metal streak artifacts in x-ray computed tomography using a transmission maximum a posteriori algorithm. *IEEE Transactions on Nuclear Science*, **47**, 997-981. doi:10.1109/23.856534

[24] Robertson, D.D., Yuan, J., Wang, G., *et al*. (1997) Total hip prosthesis metal-artifact suppression using iterative deblurring reconstruction. *Journal of Computer Assisted Tomography*, **21**, 293-298. doi:10.1097/00004728-199703000-00024

[25] Gomi, T., Hirano, H. and Umeda, T. (2009) Evaluation of the X-ray digital linear tomosynthesis reconstruction processing method for metal artifact reduction. *Computerized Medical Imaging and Graphics*, **33**, 257-274. doi:10.1016/j.compmedimag.2009.01.004

[26] Stevens, G.M., Fahrig, R. and Pelc, N.J. (2001) Filtered backprojection for modifying the impulse response of circular tomosynthesis. *Medical Physics*, **28**, 372-379. doi:10.1118/1.1350588

[27] Stevens, G.M., Birdwell, R.L., Beaulieu, C.F., *et al*. (2003) Circular tomosynthesis: potential in imaging of breast and upper cervical spine-preliminary phantom and in vitro study. *Radiology*, **228**, 569-575. doi:10.1148/radiol.2282020295

[28] Gomi, T., Yokoi, N. and Hirano, H. (2007) Evaluation of digital linear tomosynthesis imaging of the temoromandibular joint: initial clinical experience and evaluation. *Dentomaxillofac Radiology*, **36**, 514-521. doi:10.1259/dmfr/26026102

[29] Yankelevitz, D.F., Reeves, A.P., Kostis, W.J., Zhao, B. and Henschke, C.I. (2000) Small pulmonary nodules: volumetrically determined growth rates based on CT evaluation. *Radiology*, **217**, 251-256.

[30] Vikgren, J., Zachrisson, S., Svalkvist, A., *et al*. (2008) Comparison of chest tomosynthesis and chest radiography for detection of pulmonary nodules: human observer study of clinical cases. *Radiology*, **249**, 1034-1041. doi:10.1148/radiol.2492080304

[31] Zachrisson, S., Vikgren, J., Svalkvist, A., *et al*. (2009) Effect of clinical experience of chest tomosynthesis on detection of pulmonary nodules. *Acta Radiologica*, **50**, 884-891. doi:10.1080/02841850903085584

[32] Dobbins, J.T. III, Mcadams, H.P., Song, J.W., *et al*. (2008) Digital tomosynthesis of the chest for lung nodule detection: interim sensitivity results from an ongoing NIH-sponsored trial. *Medical Physics*, **35**, 2554-2557. doi:10.1118/1.2937277

[33] Johnsson, A.A., Vikgren, J., Salkvist, A., *et al*. (2010) Overview of two years of clinical experience of chest tomosynthesis at sahlgrenska university hospital. *Radiation Protection Dosimetry*, **139**, 124-129. doi:10.1093/rpd/ncq059

[34] Godwin, J.D. (1983) The solitary pulmonary nodule. *Radiologic Clinics of North America*, **21**, 709-721.

[35] Littleton, J.T. (1983) Pluridirectional tomography in diagnosis and management of early bronchogenic carcinoma. In: Little, J.T. and Durizch, M.L., *Sectional imaging methods. A comparison*, University Park Press, Baltimore, 155.

[36] Siegelman, S.S., Khouri, N.F., Leo, F.P., *et al*. (1986) Solitary pulmonary nodules. CT assessment. *Radiology*, **160**, 307-312.

[37] Siegelman, S.S., Zerhouni, E,A., Loe, F.P., *et al*. (1980) CT of the solitary pulmonary nodule. *American Journal of Roentgenology*, **135**, 1-13.

[38] Zerhouni, E.A., Caskey, C. and Khouri, N.F. (1988) The pulmonary nodules. *Seminars in Ultrasound, CT, and MR*, **9**, 67-78.

[39] Fraser, R.G., Hickey, N.M., Niklason, L.T., *et al*. (1986) Calcification in pulmonary nodules. Detection with dual-energy digital radiography. *Radiology*, **160**, 595-601.

[40] McLendon, R.E., Roggli, V.L., Foster, W.L. Jr., *et al*. (1985) Carcinoma of the lung with osseous stromal metaplasia. *Archives of Pathology & Laboratory Medicine*, **109**, 1051-1053.

[41] O'Keefe, M.E. Jr., Good, C.A. and McNonald, J.R. (1957) Calcification in solitary nodules of the lung. *American Journal of Roentgenology*, **77**, 1023-1033.

[42] Burgener, F.A. and Kormano, M. (1991) Differential diagnosis in conventional radiology. Thieme Verlag, Berlin.

[43] Brody, W.R., Butt, G., Hall. A. and Macovski, A. (1981) A method for selective tissue and bone visualization using dual-energy scanned projection radiography. *Medical Physics*, **8**, 659-667. doi:10.1118/1.594957

[44] Hickey, N.M., Niklason, L.T., Sabbagh, E., *et al.* (1987)

Dual-energy digital radiographic quantification of calcium in simulated pulmonary nodules. *American Journal of Roentgenology*, **148**, 19-24.

[45] Ishigaki, T., Sakuma, S., Horikawa, Y., *et al*. (1986) One-shot dual-energy subtraction imaging. *Radiology*, **161**, 271-273.

[46] Ishigaki, T., Sakuma, S. and Ikeda, M. (1988) One-shot dual-energy subtraction chest imaging with computed radiography. *Radiology*, **168**, 67-72.

[47] Nishitani, H., Umezu, Y., Ogawa, K., *et al*. (1986) Dual-energy projection radiography using condenser X-ray generator and digital radiography apparatus. *Radiology*, **161**, 533-535.

[48] Gomi, T., Nakajima, M., Fujiwara, H., *et al*. (2011) Comparison of chest dual-energy subtraction digital tomosynthesis imaging and dual-energy subtraction radiography to detect simulated pulmonary nodules with and without calcifications: a phantom study. *Academic Radiology*, **18**, 191-196. doi:10.1016/j.acra.2010.09.021

Appendix A

Modified FBP Algorithm

The 3D Fourier transform of the 3D volume data generated by the backprojection is based on the following **Eq.1**:

$$F\left(w_x, w_y, w_z\right) = \iiint f(x,y,z)\cdot\exp\left\{-j(w_x\cdot x + w_y\cdot y + w_z\cdot z)\right\}dx\cdot dy\cdot dz \quad (1)$$

where $f\left(x,y,z\right)$ is the simple backprojection intermediate image, and x, y, and z are real numbers. The meaning of the filtering process performed in 3D Fourier space is described below, and it is mathematically expressed by the following **Eq.2**:

$$FM\left(w_x, w_y, w_z\right) = F\left(w_x, w_y, w_z\right)\cdot M\left(w_x, w_y, w_z\right) \quad (2)$$

where $FM\left(w_x, w_y, w_z\right)$ is the filtered 3D Fourier distribution image, and $M\left(w_x, w_y, w_z\right)$ is a function representing filter characteristics. The filtering process carried out in 3D Fourier space is to weight the 3D Fourier distribution image of complex data with the real-valued filter function M dependent on the respective frequency values. The weighting function M is compressed in the w_z direction. $M\left(w_x, w_y, w_z\right)$ is expressed by the following **Eq.3** as a product of three functions representing the filter characteristic:

$$M\left(w_x, w_y, w_z\right) = H_{prof}\left(w_z\right)\cdot H_{spec}\left(w_r\right)\cdot H_{inverse}\left(wR\right) \quad (3)$$

$H_{prof}(w_z)$ has a low-pass filter characteristic, *i.e.*, a Gaussian characteristic, which is expressed by the following **Eq.4**:

$$H_{prof}(w_z) = \exp\left(-0.693\left[\frac{w_z}{CFD}\right]^2\right) \quad (4)$$

where CFD is the frequency with the Gaussian attenuation halved.

$H_{spec}(w_r)$ has a filter characteristic which is expressed by the following **Eq.5**:

$$\begin{cases} H_{spec}(w_r) = 1 & \left(case \quad w_r < \dfrac{CFR-WFR}{2}\right) \\ H_{spec}(w_r) = \dfrac{1-\sin(w_r - CFR)\cdot\pi/WFR}{2} & \left(case \quad \dfrac{CFR-WFR}{2} < w_r < \dfrac{CFR+WFR}{2}\right) \\ H_{spec}(w_r) = 0 & \left(case \quad \dfrac{CFR+WFR}{2} < w_r\right) \end{cases} \quad (5)$$

However, $w_r = \sqrt{w_x^2 + w_y^2 + w_z^2}$. The function has a sine wave form with high-frequency components smoothly attenuated. CFR is the cut-off frequency, and WFR is the total transition frequency width of the filter strength. $\dfrac{CFR+WFR}{2}$ is the Nyquist frequency and $\dfrac{CFR-WFR}{2}$ is the no-processing region frequency. This $H_{spec}(w_r)$ removes high-frequency components from the origin of the 3D Fourier space. $H_{inverse}(wR)$ has a filter characteristic which is expressed by the following **Eq.6**:

$$H_{inverse}(\omega R) = |\omega R| \quad , \quad \omega R = \sqrt{\omega_x^2 + \omega_y^2} \quad (6)$$

The 3D back Fourier transforms the Fourier space data back to 3D volume data, having undergone Fourier space low-pass filtering. The 3D back Fourier transform is expressed by the following **Eq.7**:

$$fm(x,y,z) = \frac{1}{8}\pi^3 \iiint FM(w_x, w_y, w_z)\cdot\exp\left\{j\left(w_x\cdot x + w_y\cdot y + w_z\cdot z\right)\right\} dw_x dw_y dw_z \quad (7)$$

where **Eq.7** is the transformation from the frequency domain to the space domain. It is the inverse of the relation described by **Eq.1**.

APPENDIX B

Metal artifact processing

$H_{inverse}(wR)$ has a filter characteristic expressed by the following **Eq.8**:

$$w_{R\_temp} = W + \sqrt{w_x^2 + w_y^2}$$

$$w_{R\_norm} = \frac{w_{R\_temp}}{w_{R\_max}}$$

$$H_{inverse}(wR) = |w_{R\_norm}| \quad (8)$$

where W is the addition of a direct current component. w_{R_max} is the maximum value of a w_{R_temp} value. The characteristics in the negative direction along the horizontal axis are omitted because these are in linear symmetry about the vertical axis with the characteristics in the positive direction. $H_{spec}(w_r)\cdot H_{inverse}(wR)$ is expressed by the following **Eq.9**:

$$\begin{cases} H_{spec}(w_r)\cdot H_{inverse}(wR) = \dfrac{2_{rH}}{\pi}\left|w_{R\_norm}\right| + \sin\left(\dfrac{\pi\, r}{2_{rH}}\right) & \left(|r| \le rH\right) \\ H_{spec}(w_r)\cdot H_{inverse}(wR) = 0 & \left(|r| > rH\right) \end{cases} \quad (9)$$

rH is the Nyquist frequency $\left(\dfrac{CFR+WFR}{2}\right)$ and r is the no-processing region frequency $\left(\dfrac{CFR-WFR}{2}\right)$.

The 3D back Fourier transforms the Fourier space data back to 3D volume data, having undergone Fourier space low-pass filtering.

